Magnetic Resonance in Medicine 63:797–802 (2010)

# Interventional MRI: Tapering Improves the Distal Sensitivity of the Loopless Antenna

Di Qian,[1,2] AbdEl-Monem M. El-Sharkawy,[1] Ergin Atalar,[1,3] and Paul A. Bottomley[1,2*]

**The "loopless antenna" is an interventional MRI detector consisting of a tuned coaxial cable and an extended inner conductor or "whip". A limitation is the poor sensitivity afforded at, and immediately proximal to, its distal end, which is exacerbated by the extended whip length when the whip is uniformly insulated. It is shown here that tapered insulation dramatically improves the distal sensitivity of the loopless antenna by pushing the current sensitivity toward the tip. The absolute signal-to-noise ratio is numerically computed by the electromagnetic method-of-moments for three resonant 3-T antennae with no insulation, uniform insulation, and with linearly tapered insulation. The analysis shows that tapered insulation provides an ~400% increase in signal-to-noise ratio in trans-axial planes 1 cm from the tip and a 16-fold increase in the sensitive area as compared to an equivalent, uniformly insulated antenna. These findings are directly confirmed by phantom experiments and by MRI of an aorta specimen. The results demonstrate that numerical electromagnetic signal-to-noise ratio analysis can accurately predict the loopless detector's signal-to-noise ratio and play a central role in optimizing its design. The manifold improvement in distal signal-to-noise ratio afforded by redistributing the insulation should improve the loopless antenna's utility for interventional MRI. Magn Reson Med 63:797–802, 2010. © 2010 Wiley-Liss, Inc.**

**Key words: interventional MRI; MRI detectors; loopless antenna; signal-to-noise ratio; intravascular MRI**

The dipole-based "loopless antenna" is a minimally invasive interventional MRI detector that can be made much thinner than the cable connecting it to the scanner (1) while providing an intrinsically larger sensitive field of view (FOV) than its miniaturized solenoidal counterpart (2). The loopless antenna consists of a coaxial cable tuned to a multiple of a quarter wavelength ($\lambda/4$), with one pole formed by an extended inner conductor or "whip", whose length is tuned for minimal impedance or for resonance at the MRI frequency (3). The second pole is formed by the distal end of the cable shield (2). The cable and whip contain no discrete tuning elements, but the antenna is matched, tuned, and decoupled with circuit elements located outside of the body at the proximal end, where it interfaces to the MRI scanner. The antenna's highest sensitivity occurs at the whip/cable junction, but its sensitivity decreases toward the distal end of the whip and toward the proximal end of the cable shield (2). The loopless antenna has been utilized in experimental studies, including MR-guided angioplasty (4,5), imaging atherosclerotic plaque (6), and deep-brain stimulation (7).

IMRI devices are often electrically insulated to provide biocompatibility and mechanical stability. The insulation can affect the coupling of the device with the MRI radiofrequency transmitter and gradient magnetic fields (8), in some cases reducing the potential for heating and thereby improving device safety during MRI. To date, as is the case for many interventional MRI devices, the insulation applied to the loopless antenna is of uniform thickness over the entire device. The insulation has the side effect of significantly increasing the resonant length of the whip because the dielectric constant ($\varepsilon$) of the insulator, which is typically a biocompatible polymer, is much lower than that of the surrounding biologic tissue. While the longer whip extends the sensitivity for the loopless antenna along its long axis, the result is a reduction in sensitivity near the distal end as compared to an uninsulated antenna. This renders the distal end of the device essentially invisible under MRI.

Poor sensitivity near the tip is problematic for potential interventional applications where visualizing the distal signal distribution is important. This includes intravascular imaging of chronic total occlusion (9), where poor visibility could result in vessel perforation and difficulty in navigating the device through the vasculature. It also includes MRI-guided deep-brain-stimulation electrode placement, where poor visibility may require advancement of the device beyond the target site in order to obtain adequate signal-to-noise ratio (SNR) to visualize it (7).

Here, we report that the distal MRI sensitivity of an insulated loopless antenna can be significantly improved by tapering the insulation to increase the sensitivity near the tip. We compare the SNR at and proximal to the distal end of the tapered loopless antenna with that of uniformly insulated and uninsulated loopless antennae, using the numerical electromagnetic (EM) method-of-moments. The results are confirmed by experimental studies in phantoms and a pig aorta specimen at 3 T.

## MATERIALS AND METHODS

### Principle

By the principle of reciprocity, the sensitivity of a detector is proportional to the transverse radiofrequency

[1]Division of MR Research, Department of Radiology, Johns Hopkins University, School of Medicine, Baltimore, Maryland, USA.
[2]Department of Electrical and Computer Engineering, Johns Hopkins University, Baltimore, Maryland, USA.
[3]Department of Electrical and Electronics Engineering, Bilkent University, Ankara, Turkey.

Grant sponsor: National Institutes of Health; Grant numbers: R01 EB007829, R01 HL090728.

*Correspondence to: Paul A. Bottomley, Ph.D., Division of MR Research, Department of Radiology, Johns Hopkins University, 600 N. Wolfe St., Park Bldg Room 310, Baltimore, MD 21287. E-mail: bottoml@mri.jhu.edu

Received 11 December 2008; revised 15 May 2009; accepted 25 June 2009.
DOI 10.1002/mrm.22152
Published online in Wiley InterScience (www.interscience.wiley.com).

magnetic field produced by unit current (3). A unit current applied to the whip-cable junction of a conventional loopless antenna where the impedance, $Z_j$, is lowest results in a monotonically decreasing current distribution along the whip toward the distal tip, where the impedance, $Z_{tip}$, is highest (Fig. 1). As a consequence, the antenna's sensitivity decreases to a minimum at the tip (8). Improving the distal sensitivity of the antenna requires increasing the current there, which in turn means reducing the impedance toward the tip.

Unfortunately, options for varying the impedance along the whip are limited. Obtaining a substantial impedance reduction by increasing the conductivity of the whip conductor is impractical; excellent conductors such as gold are already used for biocompatibility reasons. However, we *can* take advantage of the significant mismatch between the dielectric constant $\varepsilon_{ins} \sim 3$ of the insulation and that of the tissue medium, $\varepsilon_{sample} \sim 80$, in which the antenna is placed because it is the surrounding medium that supports the return current paths of this dipolar antenna (2). Reducing the insulation thickness on the whip increases the distributed capacitance between the whip and the sample, thereby reducing the impedance. Moreover, a graduated reduction or tapering of the insulation thickness toward the tip decreases the distal whip impedance. This shifts the current distribution, and therefore the sensitivity, toward the antenna tip as compared to the tip sensitivity of a uniformly insulated antenna.

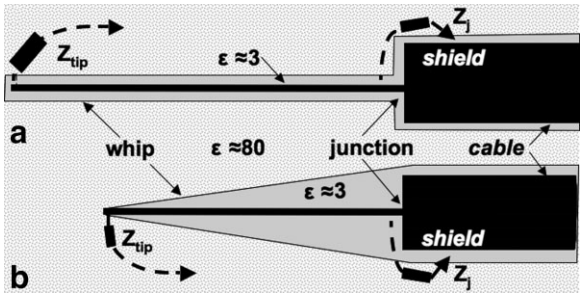


FIG. 1. The effect of uniform (**a**) and tapered (**b**) insulation on the impedance between the whip and the shield at the junction end of the loopless antenna's cable. The impedance, $Z_j$, is minimized at the junction when the antenna is tuned, resulting in maximum current, proportional to the transverse magnetic field, and maximum sensitivity at the junction (**a**). At the tip, impedance, $Z_{tip}$, is maximum, so sensitivity is at a minimum. Because the medium has a much higher dielectric constant ($\varepsilon \sim 80$) than the insulation ($\varepsilon \sim 3$), tapering in (**b**) reduces the insulation at the tip, increasing the capacitance there, which reduces $Z_{tip}$ relative to $Z_j$. This increases the current and hence the sensitivity at the distal end of the whip as compared to the uniform insulation antenna. The tuned length of the tapered whip (**b**) is also reduced by the effect that exposure to the higher dielectric constant has on the wavelength. This also improves the sensitivity near the tip by moving it physically closer to the junction.

## Loopless Antenna Models for EM Analysis

We compare the distal 3-T MRI SNR performance of loopless antennae with three different whip configurations: no insulation, uniform insulation, and tapered insulation. The coaxial cable section of each loopless antenna is modeled as a $\lambda/4$, or 39-cm length of commercially available UT-85-C semi-rigid copper cable (Microcoax Inc., Pottstown, PA), with an outer conductor diameter of 2.2mm, inner conductor diameter of 0.51mm, and a coaxial dielectric constant with $\varepsilon_{cable} = 2.2$. The cable is insulated on the outside by an 0.02mm dielectric with $\varepsilon_{ins} = 3$, consistent with that of polyethylene terephthalate heat-shrink tubing (Advanced Polymer Inc., Salem, NH). This same insulation is assumed for the whip of the insulated-whip models. The model sample load is a homogenous 0.35% saline phantom with impedance properties analogous to that of the human body ($\varepsilon_{sample} = 79$; conductivity, $\sigma_{sample} = 0.63$ S/m), as measured previously (3) and consistent with prior work (10).

The whip lengths of the three model antennae are numerically tuned to resonate under sample-loaded conditions by computing the impedance using method-of-moments EM software (FEKO, EM Software & Systems Stellenbosch, South Africa) and iterating the length until the reactance is zero (3). The outer conductors of the antennae are numerically modeled by dividing them into triangular copper elements of edge length $<\lambda_f/100$, where $\lambda_f$ is the free-space wavelength at the MRI frequency. The inner conductors are modeled as wire segments of length $<\lambda_f/1000$. Both the antenna cable dielectric and the outer cable and whip insulation are modeled using the FEKO software module for evaluating wire segment dielectrics from the specified wire radius and the dielectric constant, thickness, and loss. The uninsulated whip antenna is exposed to $\varepsilon_{sample}$ for its full length, and hence the analysis yields the shortest resonant whip length of 4 cm. An intermediate whip length of 10 cm is obtained for the antenna with 1mm-thick insulation at the junction linearly tapered to 0.025mm at the tip. A 0.5mm-thick insulation thickness was chosen for ease of fabrication for the uniformly insulated antenna: the low value of $\varepsilon_{ins}$ over its full length results in the longest whip length of 16 cm.

The absolute system SNR, $\Psi_s$ in $mL^{-1}$ $Hz^{1/2}$, for the three antennae is computed under fully relaxed conditions from (11,12):

$$\Psi_s = \frac{\sqrt{2}\omega\mu M_0 |H_+|}{\sqrt{4K_B R_{eff} T_S}} \times 10^{\frac{-NF}{20}} \quad [1]$$

where $\omega$ is the Larmor angular frequency, $\mu$ is the magnetic permeability of the sample, $M_0$ ($9.33 \times 10^{-9}$ J $mL^{-1}$ for water) is the transverse nuclear magnetization per unit sample in a main magnetic field, amplitude of static field $B_o = 3$T (13). $|H_+|$ is the magnitude of the positive circularly polarized component of the magnetic field generated by the loopless antenna with unit current; $K_B$ is Boltzmann's constant; $T_s$ is the temperature of the sample in kelvin; and *NF* is the noise figure of the MRI receiver in decibels. $R_{eff}$ is the effective noise resistance of the MRI detector, which includes the resistive losses in the coaxial cable. It can be estimated by (14):

$$R_{eff} = R_{Load} \times 10^{\alpha L/10} \quad [2]$$

where $R_{Load}$ is the input impedance of the loopless antenna, $\alpha$ is the cable attenuation coefficient (0.2 dB/m

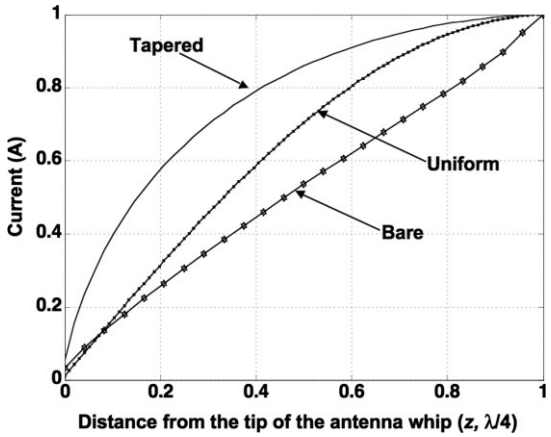


FIG. 2. The computed current distribution at a radial distance of 1 cm from the whip of the three insulated antenna models as a function of distance, *z*, along the whip relative to the tip (at $z = 0$) in units of $\lambda/4$ (= 1) in the medium. The current for the tapered coated antenna is better distributed and pushed toward the tip.

for UT-85C), $L$ is the length of the coax cable, and $\Gamma$ is the reflection coefficient between the loopless antenna and the coaxial cable.

The computation for $|H_+|$ and $R_{\text{Load}}$ for Eq. 1 is performed numerically using the EM method-of-moments FEKO software applied to the three loopless antenna models specified above, excited at the junction with unit current (3). The current distribution on the whips of each loopless antenna model is also computed using FEKO.

### Experimental Models

The computed absolute SNRs, calculated using Eq. 1 with noise figure = 0, for the three MRI loopless antenna models are validated in MRI experiments on prototype antennae immersed in a 60-L 0.35% saline phantom. The antennae are constructed from UT-85-C semirigid copper coaxial cables using polyethylene terephthalate heat-shrink tubing for the whips of the two insulated antennae. Tapering is achieved by applying different lengths of heat-shrink tubing in up to 20 layers. The antennae are tuned, matched to 50 Ω, and decoupled with a PIN (P-type, Intrinsic, N-type) diode and quarter-wave transformation by means of the circuitry described previously (3). This effectively limits radiofrequency heating during MRI to below 1°C, as shown before (3).

MRI studies were done on a Philips 3T Achieva XMR scanner (Philips Medical Systems, Cleveland, OH), with a measured noise figure of 1.1 dB. Shimming of the saline phantom using the body coil was performed prior to each scan. Absolute system SNR is measured with a fully relaxed gradient echo sequence (one echo; echo time = 6 ms, pulse repetition time = 8 sec, flip angle = 90°, bandwidth = 62.5 kHz, number of averages = 1, FOV = 8 cm, acquisition matrix, 256 × 256, 3mm slices, scan time = 34.1 min) to obtain the signal, followed by a noise image acquired with the radiofrequency and gradients switched off. The complex raw image data are exported from the scanner for calculating absolute SNR. Scan location is measured relative to the whip junction, as confirmed by scout MRI.

To determine whether the improvement in distal sensitivity afforded by tapered insulation could benefit intravascular MRI of real anatomic structures, in vitro scans are acquired from antennae in a 15-cm-long pig aorta specimen immersed in 0.35% saline. Axial images are acquired 1 cm proximal to the tip of each antenna inserted about 8 cm into the aorta, using a gradient echo sequence (one echo; echo time = 6 ms, pulse repetition time = 200 ms, flip angle = 90°, bandwidth = 62.5 kHz, number of averages = 1, FOV = 8 cm, 256 × 256 matrix, 3mm slices, scan time = 1.7 min).

## RESULTS

The current distribution along the three loopless antennae computed by FEKO is plotted from the tip to the junction of each antenna in Fig. 2. Because the whips in the three antennae have the same electrical length ($\lambda/4$) but different physical lengths as a result of the different insulation strategies, the horizontal axis is normalized to the same electrical length measured relative to the distal tip. The plot shows that the current distribution along the whip with tapered insulation is shifted toward the tip of the antenna even *after* accounting for differences in electrical length.

The SNR ($\Psi_s$ with noise figure = 0) computed from Eq. 1 at 1-cm radial distance from the three antenna whips is plotted in Fig. 3 as a function of distance from the tip, this time in millimeters. At the distal tip, the uniformly insulated antenna has much lower SNR than both the bare whip and tapered-insulation antennae. The tapered-insulation antenna's distal SNR is the highest at 28,200 $mL^{-1}$ $Hz^{1/2}$, representing a 23% improvement over the bare antenna with $\Psi_s$ = 22,900 $mL^{-1}$ $Hz^{1/2}$, which in turn is 250% higher than the uniformly insulated antenna with $\Psi_s$ = 6550 $mL^{-1}$ $Hz^{1/2}$. To compare the computed SNR with experimental measurements, a plane 1 cm proximal to the tip of the antenna whip was also chosen because the uniformly insulated antenna has

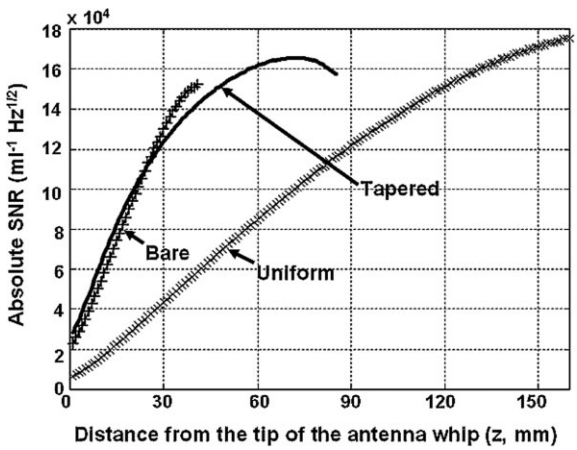


FIG. 3. The absolute SNR ($mL^{-1}$ $Hz^{1/2}$) computed at a radial distance of 1 cm from the whip as a function of distance, *z*, along the whip relative to the tip.

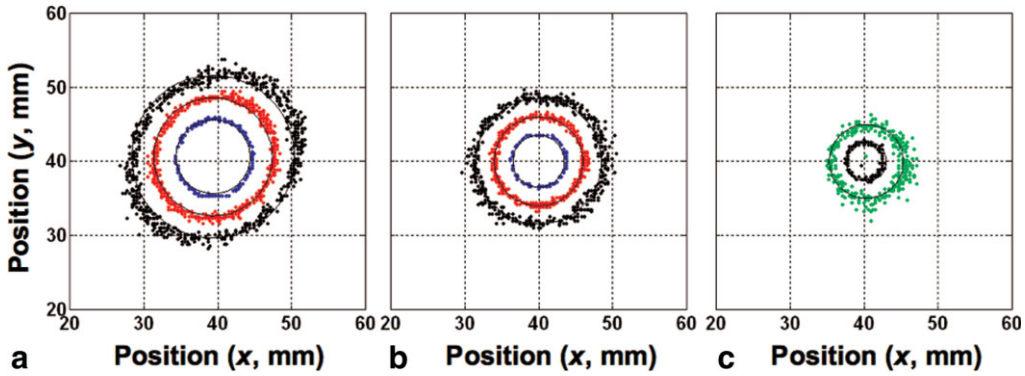


FIG. 4. Theoretical (solid, black contours) and experimental absolute SNR (blue, 150,000; red, 90,000; black, 65,000; green, 31,000; $mL^{-1}$ $Hz^{1/2}$) in the transaxial (xy) plane 1 cm from the tip of (**a**) the tapered-insulation, (**b**) the bare, and (**c**) the uniform-insulation loopless antennae immersed in 0.35% saline at 3 T. The experimental SNR data overlap computed contours with the same SNR values. The effect of the scanner noise figure is subtracted from the experimental data. The theoretical and mean experimental SNR differ by $\leq$10% in all cases.

insufficient SNR at the tip to permit reliable SNR measurements. Figure 3 shows that the tapered-insulation antenna has about a 4-fold higher computed SNR in this plane than the uniformly insulated antenna and a 20% SNR advantage over the bare antenna.

The SNR computed in the transaxial plane 1 cm proximal to the distal end of each antenna is plotted as continuous black contours in Fig. 4. The area of the 65,000 $mL^{-1}$ $Hz^{1/2}$ contour for the tapered-insulation antenna is 67% larger than the bare antenna and 16 times larger than the uniformly insulated antenna. Thus, the analysis predicts that the 4-fold SNR gain at this location translates to a computed 16-fold improvement in useable FOV for the tapered-insulation antenna as compared to a conventional uniformly insulated antenna.

The experimental absolute SNR values acquired in transaxial planes 1 cm proximal to the tip of each antenna are overlaid in Fig. 4 as scatterplots. The experimental data coincide with the computed contours for all three loopless antennae to within 5%. The excellent agreement between the computed and the experimental results is consistent with all of the losses being essentially fully and correctly accounted for by the numerical analysis, so that the experimental antennae were in fact performing as best as could be theoretically expected. The experimental data confirm the large SNR and FOV gains realized by the tapered-insulation antenna over the uniformly insulated antenna, documented above.

Figure 5 shows magnitude images in the sagittal plane acquired from the tapered and the uniformly insulated antennae in the phantom under identical conditions. The displacement and broadening of the sensitivity profile toward the distal end of the antenna afforded by tapering the insulation are clearly evident. The measured peak image SNR 1 cm from the tip of the tapered antenna is 140 as compared to 38 for the uniformly insulated antenna, a 3.7-fold increase. Experimental contours of image SNR levels in the sagittal planes are included for the two antennae (Fig. 5c,d).

Figure 6 shows axial images of the pig aorta specimen acquired 1 cm proximal to the tip of the uniform- and tapered-insulation antennae. The image from the tapered antenna reveals the outline of the pig aorta specimen, while the SNR of the uniformly insulated antenna is too poor to show any recognizable structure.

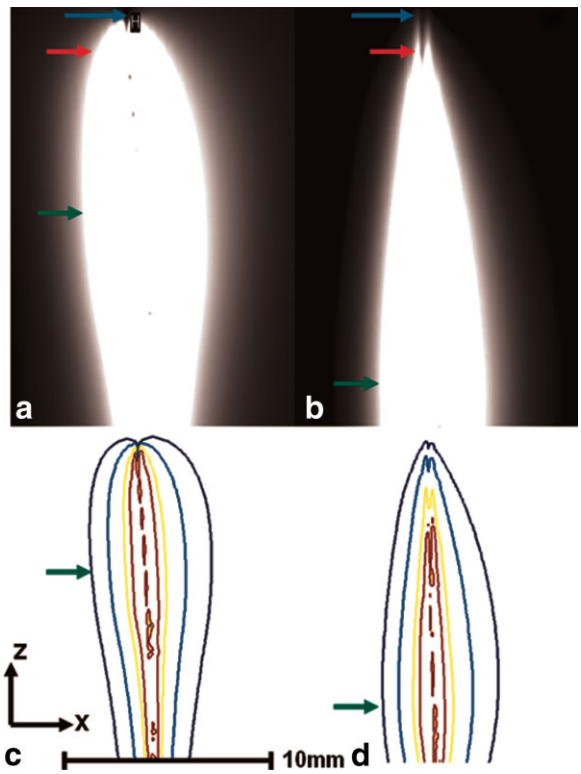


FIG. 5. Sagittal images from the phantom acquired at 3 T with (**a**) the tapered-insulation antenna and (**b**) the uniform-insulation antenna, displayed with the same contrast level. Arrows denote the antenna tips (blue) and junctions (green). The maximum image SNR level in the plane at $z = 1$ cm from the tip (red arrows) is 139 for the tapered-insulated antenna vs 38 for the uniform-insulation antenna. Shown below are corresponding contour plots of the image SNR for the (**c**) tapered-insulation and (**d**) uniform-insulation antennae (image/pixel SNR levels from center to outside are 3000, 2000, 1000, 500), with scale bar.

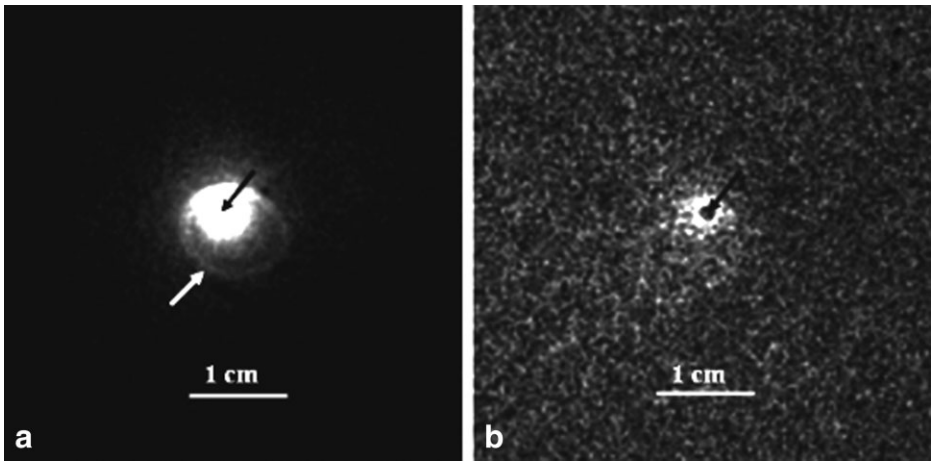


FIG. 6. 3-T transaxial images from a pig aorta in saline acquired at z = 1 cm from the antenna tip with (**a**) the tapered-insulation antenna and (**b**) the uniform-insulation antenna. The centers of the two antennae (black arrows) are the same relative to the aorta, although not concentric with it. The tapered antenna reveals the outline of the aorta (white arrow), while the uniformly insulated antenna reveals no recognizable structure.

## DISCUSSION

This study shows for the first time that the distribution of insulation on internal interventional MRI detectors can significantly affect the detector sensitivity profile and its SNR and that relatively minor manipulations of the insulating material can yield major SNR gains at desirable spatial locations. In particular, we have shown by both theoretical numerical EM analysis and by direct experimental studies that tapering the insulation on the loopless antenna brings a manifold gain in sensitivity at the distal end as compared to uniform insulation. The excellent agreement between the numerical method-of-moments EM analysis and the experimental measurements not only demonstrates the ability of such software tools to accurately predict the SNR of interventional MRI detectors but is also a direct illustration of how their incorporation into a detector design optimization process can produce large and tangible benefits to detector performance.

The distal 4-fold SNR gain realized here resulted in a corresponding 16-fold gain in effective FOV 1 cm proximal to the tip, as defined by the area of equivalent SNR contours in the transaxial plane (3). This almost quadratic dependence of the effective FOV with SNR for the loopless antenna arises from the $\sim 1/r$ dependence of the SNR (2,3) combined with the $\sim r^2$ dependence of the FOV area (3). To achieve the same SNR 1 cm from the tip of the tapered-insulation antenna using the uniformly insulated antenna, one must move proximally along the whip to about 4 cm from the tip (Fig. 3). This means that the tip of the uniformly insulated antenna would need to be inserted an extra 3 cm to obtain comparable images with the same SNR to visualize the device, thereby increasing the potential for vessel perforation or injury as compared to the tapered antenna. For the uniform antenna, such risks might preclude applications in vital areas such as the brain (7), or where insertion is limited by blood vessel size or occlusion (15). The 4-fold increase in SNR realized around the distal end by tapering the insulation should mitigate such dangers by improving device visibility. Of course, moving the sensitivity profile toward the tip by redistributing the insulation also improves tip tracking and targeting, reducing the need for additional windings (8,16) or special pulse sequences (17). It may also benefit the distal sensitivity profile of loopless antennae modified to provide intrinsically localized signals for MRI endoscopy (18).

The permittivity of the immediate surrounding material strongly influences the resonant length of the loopless antenna's whip, as evidenced by the increase in tuned whip length from 4 cm to 16 cm when the bare whip is uniformly insulated. This arises because $\lambda \approx 2\pi(\omega^2\mu\varepsilon)^{-1/2}$ (19), where $\varepsilon_{\text{ins}} = 3$ for the insulated lead as compared to $\varepsilon_{\text{r}} \approx 80$ for a whip in direct contact with body tissues or fluids. Although the insulation is only 0.5mm thick, its effect is the same as having a string of very-low-valued capacitors, representing the insulation, in series with high-valued capacitors, representing the medium, distributed along the whip. While the electrical length may be the same as that of the bare wire, the longer physical length of the insulated whip extends the size of the low-SNR region near the device tip, which is physically much farther from the high-SNR junction than is the case for the uninsulated whip.

The 10-cm resonant whip length of the tapered-insulation antenna is shorter than the 16-cm uniformly insulated whip, but this is still much longer than the bare wire's 4-cm resonant whip. Thus, a reduction in whip length that brings the tip and junction physically closer together does not alone explain the comparable SNR performance of the tapered-insulation and bare antennae (Fig. 3). The additional SNR improvement at the tip of the tapered whip arises from the redistributed current sensitivity (Fig. 2). Note also that the maximum absolute SNR of the tapered antenna at the junction is only 6.6% lower than that obtained with uniform insulation (Fig. 3). Thus, the 4-fold distal SNR gain is at negligible cost to overall antenna performance.

While we show results for linearly tapered whip insulation, nonlinear tapering is certainly an option. For example, the above considerations may suggest varying the insulation thickness as the reciprocal of, or as an exponentially decreasing function of, distance $z$ from the junction. However, our computations show that the distal SNR advantage of at least these two nonlinear tapering schemes, as compared to linear tapering, is small, while they are more difficult to implement in practice.

The present work is performed at 3 T, where we have previously demonstrated a near-quadratic SNR dependence on amplitude of static field for loopless antennae (3) and project a similar $B_o^{7/4}$ realizable SNR performance for tiny loop coils (20). At 1.5 T, the resonant whip length nearly doubles, making the length of the insulated whip less manageable, with an even larger area of low SNR near the tip. Thus, the 1.5-T loopless antenna may benefit even more from tapered insulation. On the other hand, above 3 T the distal sensitivity of the loopless antenna can benefit from both the shorter whip length resulting from the decreasing wavelength and the distal displacement of the sensitivity profile afforded by tapered insulation.

## CONCLUSION

In conclusion, tapering the insulation provides substantial increases in the distal SNR of loopless MRI antennae, dramatically improving their MRI visibility at and near the tip. The design modification is relatively simple and inexpensive to implement and does not compromise the small cross-sectional profile of the loopless antenna. The resulting benefit to performance is important to the utility of the device for interventional MRI.

## ACKNOWLEDGMENTS

We thank Dr. Bill Edelstein, Parag Karmarkar for helpful discussions, Dr. Mike Schär for providing technical support for the Philips scanner, and Dawn Ruben and Laurie Pipitone for obtaining the aorta samples.

## REFERENCES

1. Qiu B, Karmarkar P, Brushett C, Gao F, Kon R, Kar S, Atalar E, Yang X. Development of a 0.014-inch magnetic resonance imaging guidewire. Magn Reson Med 2005;53:986–990.
2. Ocali O, Atalar E. Intravascular magnetic resonance imaging using a loopless catheter antenna. Magn Reson Med 1997;37:112–118.
3. El-Sharkawy AM, Qian D, Bottomley PA. The performance of interventional loopless MRI antennae at higher magnetic field strengths. Med Phys 2008;35:1995–2006.
4. Serfaty JM, Yang X, Aksit P, Quick HH, Solaiyappan M, Atalar E. Toward MRI-guided coronary catheterization: visualization of guiding catheters, guidewires, and anatomy in real time. J Magn Reson Imaging 2000;12:590–594.
5. Yang X, Atalar E. Intravascular MR imaging-guided balloon angioplasty with an MR imaging guide wire: feasibility study in rabbits. Radiology 2000;217:501–506.
6. Shunk KA, Garot J, Atalar E, Lima JA. Transesophageal magnetic resonance imaging of the aortic arch and descending thoracic aorta in patients with aortic atherosclerosis. J Am Coll Cardiol 2001;37: 2031–2035.
7. Karmarkar PVBK, Lowe MJ, Phillips M, Steiner C, Viohl I, Nyenhuis JA, Bottomley PA, Rezai AR. An active microelectrode system for experimental MRI-guided intracranial intervention. Proc Intl Soc Mag Reson Med 2005;13:2162.
8. Susil RC, Yeung CJ, Atalar E. Intravascular extended sensitivity (IVES) MRI antennas. Magn Reson Med 2003;50:383–390.
9. Stone GW, Colombo A, Teirstein PS, Moses JW, Leon MB, Reifart NJ, Mintz GS, Hoye A, Cox DA, Baim DS, Strauss BH, Selmon M, Moussa I, Suzuki T, Tamai H, Katoh O, Mitsudo K, Grube E, Cannon LA, Kandzari DE, Reisman M, Schwartz RS, Bailey S, Dangas G, Mehran R, Abizaid A, Serruys PW. Percutaneous recanalization of chronically occluded coronary arteries: procedural techniques, devices, and results. Catheter Cardiovasc Interv 2005;66:217–236.
10. Stogryn A. Equations for calculating the dielectric constant of saline water. IEEE Trans Microwave Theory Technol 1971;19:733–736.
11. Edelstein WA, Glover GH, Hardy CJ, Redington RW. The intrinsic signal-to-noise ratio in NMR imaging. Magn Reson Med 1986;3:604–618.
12. Ocali O, Atalar E. Ultimate intrinsic signal-to-noise ratio in MRI. Magn Reson Med 1998;39:462–473.
13. Chen CN, Hoult DI. Biomedical magnetic resonance technology. Medical science series. Bristol: A. Hilger; 1989. 340 p.
14. Gardiol FE. Lossy transmission lines. Boston: Artech House; 1987. 384 p.
15. Raval AN, Karmarkar PV, Guttman MA, Ozturk C, Sampath S, DeSilva R, Aviles RJ, Xu M, Wright VJ, Schenke WH, Kocaturk O, Dick AJ, Raman VK, Atalar E, McVeigh ER, Lederman RJ. Real-time magnetic resonance imaging-guided endovascular recanalization of chronic total arterial occlusion in a swine model. Circulation 2006; 113:1101–1107.
16. Anderson KJ, Leung G, Dick AJ, Wright GA. Forward-looking intravascular orthogonal-solenoid coil for imaging and guidance in occlusive arterial disease. Magn Reson Med 2008;60:489–495.
17. Shimizu K, Mulkern RV, Oshio K, Panych LP, Yoo SS, Kikinis R, Jolesz FA. Rapid tip tracking with MRI by a limited projection reconstruction technique. J Magn Reson Imaging 1998;8:262–264.
18. Sathyanarayana S, Bottomley PA. MRI endoscopy using intrinsically localized probe. Med Phys 2009;36:908–919.
19. Pozar DM. Microwave and RF wireless systems. New York: John Wiley; 2001. 366 p.
20. Kumar A, Edelstein WA, Bottomley PA. Noise figure limits for circular loop MR coils. Magn Reson Med 2009;61:1201–1209.